

Synthesis of Freestanding Single-crystal Perovskite Films and Heterostructures by Etching of Sacrificial Water-soluble Layers

Di Lu^{1,2}, David J. Baek³, Seung Sae Hong^{2,4}, Lena F. Kourkoutis^{5,6}, Yasuyuki Hikita² &
Harold Y. Hwang^{2,4}

¹ *Department of Physics, Stanford University, Stanford, California 94305, USA*

² *Stanford Institute for Materials and Energy Sciences, SLAC National Accelerator
Laboratory, Menlo Park, California 94025, USA*

³ *School of Electrical and Computer Engineering, Cornell University, Ithaca, NY
14853, USA*

⁴ *Department of Applied Physics, Stanford University, Stanford, California 94305,
USA*

⁵ *School of Applied and Engineering Physics, Cornell University, Ithaca, NY 14853,
USA*

⁶ *Kavli Institute at Cornell for Nanoscale Science, Cornell University, Ithaca, NY
14853, USA*

The ability to create and manipulate materials in two-dimensional (2D) form has repeatedly had transformative impact on science and technology. In parallel with the exfoliation and stacking of intrinsically layered crystals¹⁻⁵, atomic-scale thin film growth of complex materials has enabled the creation of artificial 2D heterostructures with novel functionality⁶⁻⁹ and emergent phenomena, as seen in perovskite heterostructures¹⁰⁻¹². However, separation of these layers from the growth substrate has proven challenging, limiting the manipulation capabilities of these heterostructures with respect to exfoliated materials. Here we present a general method to create freestanding perovskite membranes. The key is the epitaxial growth of water-soluble $\text{Sr}_3\text{Al}_2\text{O}_6$ on perovskite substrates, followed by *in situ* growth of films and heterostructures. Millimetre-size single-crystalline membranes are produced by etching the $\text{Sr}_3\text{Al}_2\text{O}_6$ layer in water, providing the opportunity to transfer them to arbitrary substrates and integrate them with heterostructures of semiconductors and layered compounds^{13,14}.

While naturally layered crystals provide intrinsic periodic interfaces for mechanical separation, typically via van der Waals bonding, the generalized synthesis of freestanding membranes from a host carrier essentially requires the creation of an interface to generate bonding anisotropy, to which a force is applied to preferentially break these bonds. The “smart-cut” technique for silicon-on-insulator technology employs an ion-implanted layer confined to a fixed depth from the bulk Si surface, which partially breaks the sp^3 covalent bonding within this layer to form a mechanically cleavable plane¹⁵. As another example, GaN films grown on transparent substrates can be released by absorbing high-power laser irradiation through the substrate, melting the

region close to the interface, as used to fabricate substrates for blue light-emitting diodes¹⁶. Despite their success in electronics applications, a major drawback of these physical release methods is the inevitable structural damage induced, especially in the limit of thin membranes. By contrast, the chemical release method, which involves membrane growth on a sacrificial layer followed by selective etching, is typically less destructive and retains the structural quality of the released membranes. A seminal example is the growth of single crystal elemental metal membranes on NaCl crystals, which act as the sacrificial layer¹⁷ released by dissolution in water¹⁸. However, for more complex binary or ternary materials, the selection of both the sacrificial layer and the etchant is restricted by many parameters, such as: etchant selectivity, lattice symmetry and matching for epitaxial growth, and stability of the sacrificial layer during the target membrane growth (often at high temperatures under varying thermodynamic conditions). As a result, there are a limited number of binary or ternary single crystalline membranes produced through this approach¹⁹. Examples include GaAs membranes released using AlAs as the sacrificial layer²⁰, and SrRuO₃ membranes from SrTiO₃ sacrificial substrates^{21, 22}. Both cases utilize the extreme chemical stability of the membrane to the hydrofluoric acid used as the etchant – our aim is to develop a “universal” sacrificial layer and etchant combination, which can be applied to virtually all perovskites and their heterostructures.

To this end, we have developed the epitaxial growth and selective etching of Sr₃Al₂O₆ as a hygroscopic oxide sacrificial thin film layer. The isostructural compound Ca₃Al₂O₆ is often a few percent component of Portland cement, forming in the clinker and contributing to binding when hydrated²³. In crystalline form, the hydrogarnet

$\text{Ca}_3\text{Al}_2(\text{OH})_{12}$ is only weakly soluble in water due to strong Ca-O bonding. However, by substituting Sr for Ca, the solubility can be greatly increased. As shown in Fig. 1a, $\text{Sr}_3\text{Al}_2\text{O}_6$ forms a cubic unit cell (space group $P\bar{a}3$) with lattice constant $a = 15.844 \text{ \AA}$, which closely matches four unit cells of the most representative perovskite substrate SrTiO_3 ($a_{\text{STO}} = 3.905 \text{ \AA}$, $4 \times a_{\text{STO}} = 15.620 \text{ \AA}$)²⁴. Despite the apparent structural complexity, with 264 atoms in the unit cell, $\text{Sr}_3\text{Al}_2\text{O}_6$ shares a similar lattice to SrTiO_3 , as is clear from the two structures projected onto the (001)-plane (Fig. 1b, only two atomic layers are shown for $\text{Sr}_3\text{Al}_2\text{O}_6$). Compared to a 4×4 SrTiO_3 lattice, 75 % of the $\text{Sr}_3\text{Al}_2\text{O}_6$ oxygen sub-lattice is reproduced from SrTiO_3 with small offsets, and the remaining 25 % can be regarded as regularly positioned vacancies. Similarly, the $\text{Sr}_3\text{Al}_2\text{O}_6$ cation sub-lattice can be constructed by introducing ordered cation vacancies in the SrTiO_3 cation sub-lattice.

This close resemblance in lattice forms the strong basis for the epitaxial growth of $\text{Sr}_3\text{Al}_2\text{O}_6$ on SrTiO_3 . Figure 1d shows the 2θ - ω X-ray diffraction (XRD) pattern of an 80 nm $\text{Sr}_3\text{Al}_2\text{O}_6$ film grown by pulsed laser deposition (PLD) on a SrTiO_3 (001) substrate (see Methods), clearly indicating single phase, epitaxially oriented $\text{Sr}_3\text{Al}_2\text{O}_6$. However, by simply immersing the $\text{Sr}_3\text{Al}_2\text{O}_6 / \text{SrTiO}_3$ (001) structure into de-ionized water at room temperature, the $\text{Sr}_3\text{Al}_2\text{O}_6$ layer was completely removed in a few seconds, as shown in Fig. 1e. A key aspect of the Al-O network in $\text{Sr}_3\text{Al}_2\text{O}_6$ is that it consists of discrete 12-membered $\text{Al}_6\text{O}_{18}^{18-}$ rings ($\sim 10 \text{ \AA}$ in diameter), composed of six AlO_4 tetrahedra (Fig. 1c). These rings readily hydrolyze in water, unlike other aluminates with continuous Al-O networks. Therefore, the underlying SrTiO_3 surface is completely free of any residues, recovering the atomically flat SrTiO_3 surface

topography characterized by perovskite unit cell steps, as seen by atomic force microscopy (AFM) in Fig. 1f.

The next important question is whether the $\text{Sr}_3\text{Al}_2\text{O}_6$ thin film surface can act as a template for subsequent atomic scale perovskite growth. Firstly we note indications that the $\text{Sr}_3\text{Al}_2\text{O}_6$ surface preserves the perovskite step-and-terrace structure of the underlying SrTiO_3 substrate, as seen by AFM scans taken immediately after growth (Fig. 2a,b) – the bare surface degrades on the minutes timescale due to atmospheric humidity. Secondly, in this growth regime the $\text{Sr}_3\text{Al}_2\text{O}_6$ film is deposited in the layer-by-layer growth mode, for which the thickness can be controlled by monitoring reflection high-energy electron diffraction (RHEED) oscillations (Fig. 2c). Note that one oscillation corresponds to $\frac{1}{4}$ of the $\text{Sr}_3\text{Al}_2\text{O}_6$ unit cell, i.e. the perovskite equivalent subunit. For this film, 10 SrTiO_3 unit cells (~ 4 nm) were deposited on top of the $\text{Sr}_3\text{Al}_2\text{O}_6$ film by *in situ* target exchange. High quality layer-by-layer growth of the SrTiO_3 is evident, as well as a stable atomically flat surface (inset to Fig. 2c). The preservation of the high surface quality can also be seen in the RHEED patterns shown in Fig. 2d,e taken at the end of $\text{Sr}_3\text{Al}_2\text{O}_6$ and SrTiO_3 growth, respectively.

Based on these developments, we proceed to discuss the fabrication of large-scale freestanding perovskite membranes. Various perovskite thin films were grown on $\text{Sr}_3\text{Al}_2\text{O}_6$ buffer layers, including SrTiO_3 , $\text{La}_{0.7}\text{Sr}_{0.3}\text{MnO}_3$ (pseudocubic $a_{\text{LSMO}} = 3.868$ Å), and their superlattices (SL). These heterostructures were immersed in de-ionized water at room temperature to separate the films from their substrates. To mechanically stabilize the films and to facilitate the transfer of the released membranes, an elastomer support layer was formed on the heterostructure surface before release (Fig. 3a; see

Methods). Optical microscope images of various millimetre-scale freestanding membranes as released on the polydimethylsiloxane (PDMS) support layers²⁵ are shown in Fig. 3b. By using a commercial screen protector sheet (silicone-coated polyethylene terephthalate, silicone/PET) as the support²⁶, the membranes were successfully released and transferred onto silicon wafers, after which the support layer was fully removed by subsequent heating. Both optical and scanning electron microscope (SEM) images (Fig. 3c) show that the surfaces of the transferred oxide membranes are uniform and intact, even down to few nanometre thicknesses. Further AFM profilometry measurements confirmed that the membrane thickness matches the originally grown thickness to within 2 % error, consistent with the residue-free $\text{Sr}_3\text{Al}_2\text{O}_6$ removal by water etching (Fig. 1e,f).

All the transferred oxide membranes were single crystalline as confirmed by XRD. Representative reciprocal space maps (RSM) of the SrTiO_3 and $\text{La}_{0.7}\text{Sr}_{0.3}\text{MnO}_3$ films transferred onto PDMS supports around the (103) peak are presented in Fig. 4a-d, showing that the crystalline structure is preserved both before and after the release and transfer processes. The relaxed state of the top SrTiO_3 and $\text{La}_{0.7}\text{Sr}_{0.3}\text{MnO}_3$ films suggests high lattice flexibility of the $\text{Sr}_3\text{Al}_2\text{O}_6$, which renders it responsive to the strain from the top layers, and showing different lattice constants in each case (Fig. 4a,c). A further important issue we wished to address is whether intricate heterostructures could be maintained and released in membrane form, in addition to single component films. For this the atomic scale structural coherency of freestanding oxide superlattices was examined by cross-sectional high-angle annular dark field (HAADF) imaging using scanning transmission electron microscopy (STEM). The HAADF-STEM images of

epitaxial and transferred SL samples [with 12 SrTiO₃ (5 unit cell) / La_{0.7}Sr_{0.3}MnO₃ (5 unit cell) repeats] in Fig. 4e,f show that the atomically controlled SL²⁷ preserves its coherent structure after transfer, free from further intermixing or defect formation during the release process. Higher-resolution images of the Sr₃Al₂O₆/ SrTiO₃ (001) and the SL / Sr₃Al₂O₆ interfaces (Fig. 4g,h) show close correspondence to Fig. 1b. The rhombic motifs show the Sr atoms in Sr₃Al₂O₆ projected along the [100] orientation. The surface quality and crystallinity were also examined before and after transfer of SL samples (Supplementary Figs. 1, 2). The arithmetic surface roughness changed from 0.17 nm to 0.29 nm, and the rocking curve full-width-half-maximum (FWHM) showed a broadening from 0.07° to 0.20° before and after the film transfer process. We note that contributions to this broadening likely arise from macroscopic distortions of the freestanding superlattice (on PDMS support). The local surface flatness is comparable to those observed typically in oxide nanosheets³, but over millimetre scales even for this complex SL.

In addition to the structural evolution, we examined the transport and magnetic properties of La_{0.7}Sr_{0.3}MnO₃ and SL films before and after release. For single layer La_{0.7}Sr_{0.3}MnO₃ films, the physical properties were preserved, and even enhanced, in terms of the Curie temperature (T_C) and residual resistivity (Fig. 5a,b). This change upon release is considerably more dramatic for the SL sample. As seen from Fig. 5c,d, the peak in resistivity, typical for ultrathin SLs^{27, 28}, increases by ~ 40 K. Strikingly, the saturation magnetization at low temperatures is apparently doubled for the freestanding SL (Fig. 5e,f). While the microscopic origin of these phenomena is unclear, the known sensitivity of La_{0.7}Sr_{0.3}MnO₃ to strain²⁹, enhanced at interfaces in ultrathin SLs, shows

that the strain relaxation during the film release process (Supplementary Fig. 2) can have substantial impact on the physical properties.

These results demonstrate that the use of $\text{Sr}_3\text{Al}_2\text{O}_6$ as an epitaxial sacrificial layer presents an exciting general approach for producing 2D crystalline membranes of perovskite oxides, one of the largest oxide families with a broad range of important physical and chemical properties. The geometry, as well as the large lateral area, is ideal for probing various phenomena including thermal transport, the continuous application of strain, and fabricating oxide electrochemical³⁰ and electromechanical devices³¹. We note that even highly moisture-sensitive perovskites can be incorporated, simply by using ultrathin protective layers in the membranes. For example, we find that the timescale for dissolving the $\text{Sr}_3\text{Al}_2\text{O}_6$ itself can be varied from ~ 1 second for an unprotected film (Fig. 1e), to ~ 1 day for buried layers of intermediate thickness (20 – 40 nm), to long-term stability for thinner layers. Considering the atomically controlled growth techniques already well developed in the field, freestanding membranes of oxide single crystals and heterostructures offer a unique opportunity to combine thin film heterostructure approaches with semiconductor device architectures³², flexible electronics³³, and the growing family of exfoliated 2D materials¹⁴.

References:

1. Novoselov, K. S. *et al.* Electric field effect in atomically thin carbon films. *Science* **306**, 666-669 (2004).

2. Dean, C. R. *et al.* Hofstadter's butterfly and the fractal quantum Hall effect in moiré superlattices. *Nature* **497**, 598-602 (2013).
3. Osada, M. & Sasaki, T. Two-dimensional dielectric nanosheets: novel nanoelectronics from nanocrystal building blocks. *Adv. Mater.* **24**, 210-228 (2012).
4. Xu, M., Lian, T., Shi, M. & Chen, H. Graphene-like two-dimensional materials. *Chem. Rev.* **113**, 3766-3798 (2013).
5. Butler, S. Z. *et al.* Progress, challenges, and opportunities in two-dimensional materials beyond graphene. *ACS Nano* **7**, 2898-2926 (2013).
6. Wang, Q.-Y. *et al.* Interface-induced high-temperature superconductivity in single unit-cell FeSe films on SrTiO₃, *Chin. Phys. Lett.* **29**, 037402 (2012).
7. Chang, C. Z. *et al.* Experimental observation of the quantum anomalous Hall effect in a magnetic topological insulator. *Science* **340**, 167-170 (2013).
8. Shishido, H. *et al.* Tuning the dimensionality of the heavy fermion compound CeIn₃. *Science* **327**, 980-983 (2010).
9. Bode, M. *et al.* Chiral magnetic order at surfaces driven by inversion asymmetry. *Nature* **447**, 190-193 (2007).
10. Caviglia, A. D. *et al.* Electric field control of the LaAlO₃/SrTiO₃ interface ground state. *Nature* **456**, 624-627 (2008).
11. Mannhart, J. & Schlom, D. G. Oxide interfaces-an opportunity for electronics. *Science* **327**, 1607-1611 (2010).

12. Hwang, H. Y. *et al.* Emergent phenomena at oxide interfaces. *Nature Mater.* **11**, 103-113 (2012).
13. Alferov, Zh. I. *Semiconductor heterostructures: physical processes and applications.* MIR Publishers, Moscow (1989).
14. Geim, A. K. & Grigorieva, I. V. Van der Waals heterostructures. *Nature* **499**, 419-425 (2013).
15. Bruel, M. Application of hydrogen ion beams to Silicon On Insulator material technology. *Nucl. Instrum. Methods Phys. Res., Sect. B* **108**, 313-319 (1996).
16. Wong, W. S., Sands, T. & Cheung, N. W. Damage-free separation of GaN thin films from sapphire substrates. *Appl. Phys. Lett.* **72**, 599-601 (1998).
17. Matthews, J. W. Growth of face-centered-cubic metals on sodium chloride substrates. *J. Vac. Sci. Technol.* **3**, 133-145 (1966).
18. Catlin, A. & Walker, W. P. Mechanical properties of thin single-crystal gold films. *J. App. Phys.* **31**, 2135-2139 (1960).
19. Rogers, J. A., Lagally M. G. & Nuzzo R. G. Synthesis, assembly and applications of semiconductor nanomembranes. *Nature* **477**, 45-53 (2011).
20. Yablonovitch, E., Gmitter, T., Harbison, J. P. & Bhat, R. Extreme selectivity in the lift-off of epitaxial GaAs films. *Appl. Phys. Lett.* **51**, 2222-2224 (1987).

21. Gan, Q., Rao, R. A., Eom, C. B., Garrett, J. L. & Lee, M. Direct measurement of strain effects on magnetic and electrical properties of epitaxial SrRuO₃ thin films. *Appl. Phys. Lett.* **72**, 978-980 (1998).
22. Paskiewicz, D. M., Sichel-Tissot, R., Karapetrova, E., Stan, L. & Fong, D. D. Single-Crystalline SrRuO₃ Nanomembranes: A Platform for Flexible Oxide Electronics. *Nano Lett.* **16**, 534-542 (2016).
23. Bullard, J. W. *et al.* Mechanisms of cement hydration. *Cem. Concr. Res.* **12**, 1208-1223 (2011).
24. Alonso, J. A., Rasines, I. & Soubeyroux, J. L. Tristrontium dialuminum hexaoxide: an intricate superstructure of perovskite. *Inorg. Chem.* **29**, 4768-4771 (1990).
25. Kim, K. S. *et al.* Large-scale pattern growth of graphene films for stretchable transparent electrodes. *Nature* **457**, 706-710 (2009).
26. Chen, X. *et al.* High-quality and efficient transfer of large area graphene films onto different substrates. *Carbon* **56**, 271-278 (2013).
27. Kourkoutis, L. F., Song, J. H., Hwang, H. Y. & Muller, D. A. Microscopic origins for stabilizing room-temperature ferromagnetism in ultrathin manganite layers. *Proc. Natl. Acad. Sci.* **107**, 11682-11685 (2010).
28. Izumi, M., Ogimoto, Y., Manako, T., Kawasaki, M. & Tokura, Y. Interface effect and its doping dependence in La_{1-x}Sr_xMnO₃/SrTiO₃ superlattices. *J. Phys. Soc. Jpn.* **71**, 2621-2624 (2002).

29. Thiele, C., Dorr, K., Bilani, O., Rodel, J. & Schultz, L. Influence of strain on the magnetization and magnetoelectric effect in $\text{La}_{0.7}\text{A}_{0.3}\text{MnO}_3/\text{PMN-PT}(001)$ ($\text{A} = \text{Sr}, \text{Ca}$). *Phys. Rev. B* **75**, 054408 (2007).
30. Evans, A., Bieberle-Hütter, A., Rupp, J. L. M. & Gauckler, L. J. Review on microfabricated micro-solid oxide fuel cell membranes. *J. Power Sources* **194**, 119-129 (2009).
31. Wang, Z. L. & Song, J. Piezoelectric nanogenerators based on zinc oxide nanowire arrays. *Science* **312**, 242-246 (2006).
32. Ko, H. *et al.* Ultrathin compound semiconductor on insulator layers for high-performance nanoscale transistors. *Nature* **468**, 286-289 (2010).
33. Nomura, K. *et al.* Room-temperature fabrication of transparent flexible thin-film transistors using amorphous oxide semiconductors. *Nature* **432**, 488-492 (2004).

Methods

Epitaxial film fabrication: TiO_2 -terminated SrTiO_3 (001) substrates were pre-annealed at an oxygen partial pressure $p(\text{O}_2)$ of 5×10^{-6} Torr for 30 min at 950°C to achieve sharp step-and-terrace surfaces. The $\text{Sr}_3\text{Al}_2\text{O}_6$ layer was grown first on top of the SrTiO_3 (001) substrate followed by the growth of thin film (SrTiO_3 or $\text{La}_{0.7}\text{Sr}_{0.3}\text{MnO}_3$) or their SL by PLD using a 248 nm KrF excimer laser. The $\text{Sr}_3\text{Al}_2\text{O}_6$ layer was grown at a substrate temperature T_g of 700°C and $p(\text{O}_2) = 1 \times 10^{-6}$ Torr, using 1.25 J/cm^2 laser fluence and 4 mm^2 laser spot size on the target. The $\text{Sr}_3\text{Al}_2\text{O}_6$

polycrystalline target was prepared by sintering a mixture of stoichiometric amounts of SrCO_3 and Al_2O_3 at $1350\text{ }^\circ\text{C}$ for 24 hours, with two intermediate grinding and pelletizing steps. The $\text{Sr}_3\text{Al}_2\text{O}_6$ thickness of $\sim 20\text{ nm}$ was measured by AFM for 50 RHEED oscillations, indicating that four RHEED oscillations correspond to the deposition of one unit cell of $\text{Sr}_3\text{Al}_2\text{O}_6$. The SrTiO_3 films and the SL were grown at $T_g = 900\text{ }^\circ\text{C}$ and $p(\text{O}_2) = 1 \times 10^{-6}\text{ Torr}$, using 0.35 J/cm^2 laser fluence and 11 mm^2 laser spot size on a single crystal SrTiO_3 target²⁷. The $\text{La}_{0.7}\text{Sr}_{0.3}\text{MnO}_3$ single layer films were grown at $T_g = 700\text{ }^\circ\text{C}$ and $p(\text{O}_2) = 1 \times 10^{-5}\text{ Torr}$, using 0.35 J/cm^2 laser fluence and 11 mm^2 laser spot size on a polycrystalline target. The entire structure was grown in the layer-by-layer mode as seen from continuous RHEED oscillations for all layers during growth.

Release of freestanding membranes: Approximately 0.1 mm thick PDMS was spread on a clean silicon wafer to make flat PDMS sheets. The oxide heterostructure surface was adhered onto the PDMS surface. The structure was immersed into room temperature filtered de-ionized water to dissolve the $\text{Sr}_3\text{Al}_2\text{O}_6$ layer (Fig. 3a). For transferring the freestanding oxide membranes to other substrates such as silicon, the samples were attached to commercial screen protector sheets (silicone coated PET) and released in the same manner. After etching in water, the supports with freestanding membranes were placed on silicon wafers. The membranes remained on the wafers after detaching the supports by heating at $70\text{ }^\circ\text{C}$ for 10 minutes (Fig. 3a).

Characterisation: The SEM images were taken using an FEI Nova NanoSEM. The AFM images were acquired in tapping mode. Due to the highly hygroscopic nature of $\text{Sr}_3\text{Al}_2\text{O}_6$, AFM images of $\text{Sr}_3\text{Al}_2\text{O}_6$ were taken immediately after the sample growth,

with maximum air exposure time of approximately 10 minutes (Fig. 2b). The XRD data were taken using a monochromated Cu-K_{α1} source. Cross-sectional TEM specimens were prepared using the standard focused ion beam (FIB) lift-out process on a FEI Strata 400 STEM FIB equipped with an Omniprobe AutoProbe 200. In order to study the structure of a freestanding SL film, the film was first transferred onto a silicon wafer as described above. The van der Waals forces between the freestanding film and the silicon substrate were sufficient to subsequently prepare a cross-sectional TEM specimen using the same FIB lift-out process. HAADF-STEM images were obtained on a 200 keV FEI Tecnai F20 SuperTWIN STEM and a 5th-order aberration corrected 100 keV Nion UltraSTEM. The magnetization data were measured using a superconducting quantum interference device (SQUID) magnetometer with in-plane magnetic field. The freestanding membranes were transferred onto thin PDMS sheets for magnetization measurements. The magnetotransport measurements were conducted in a four-point geometry with gold contacts under perpendicular magnetic field. The freestanding membranes were transferred to polished SrTiO₃ single crystal substrates as the support template for transport measurements.

Acknowledgements

This work was supported by the Department of Energy, Office of Basic Energy Sciences, Division of Materials Sciences and Engineering, under contract DE-AC02-76SF00515 (heterostructure synthesis); the Gordon and Betty Moore Foundation's EPiQS Initiative through Grant GBMF4415 (development of release and transfer

processes); and the Cornell Center for Materials Research with funding from the NSF MRSEC program DMR-1120296 (electron microscopy).

Author contributions:

D.L. and S.S.H. fabricated and characterised the epitaxial heterostructures and freestanding membranes. D.J.B. and L.F.K. measured and analysed the STEM data. D.L., Y.H., and H.Y.H designed the experiment and wrote the manuscript, with input from all authors.

Reprints and permissions information is available at www.nature.com/reprints.

Competing financial interests statement

The authors declare no competing financial interests.

Corresponding Authors

Correspondence and requests for materials should be addressed to Yasuyuki Hikita, hikita@stanford.edu and Harold Y. Hwang, hyhwang@stanford.edu.

This letter has supplementary information.

Figure Legends

Fig. 1 Crystal structure and epitaxial growth of $\text{Sr}_3\text{Al}_2\text{O}_6$. **a**, Cubic lattice structure of $\text{Sr}_3\text{Al}_2\text{O}_6$. **b**, (top) Top 1/4 of the $\text{Sr}_3\text{Al}_2\text{O}_6$ unit cell projected onto the (001)-plane. Dashed circles indicate vacancy sites. (bottom) 4×4 unit cells of the SrTiO_3 crystal structure projected onto the (001)-plane. **c**, $\text{Al}_6\text{O}_{18}^{18-}$ rings in $\text{Sr}_3\text{Al}_2\text{O}_6$ consisting of AlO_4 tetrahedra. **d**, XRD 2θ - ω scan of an 80 nm $\text{Sr}_3\text{Al}_2\text{O}_6$ film on a SrTiO_3 (001) substrate. **e**, A masked section of a 200 nm-thick $\text{Sr}_3\text{Al}_2\text{O}_6$ film grown on (001) SrTiO_3 before (top) and after (bottom) water treatment. **f**, AFM image of the surface morphology after dissolving the $\text{Sr}_3\text{Al}_2\text{O}_6$ film by water treatment, showing the recovered SrTiO_3 step-and-terrace structure.

Fig. 2 $\text{Sr}_3\text{Al}_2\text{O}_6$ surface structure. AFM image of the surface morphology of a $\text{Sr}_3\text{Al}_2\text{O}_6$ (20 nm) / SrTiO_3 (001) sample **a**, 4 minutes and **b**, 10 minutes after exposure to air. The line profiles indicate that the perovskite unit cell steps of the substrate are preserved at the $\text{Sr}_3\text{Al}_2\text{O}_6$ surface. **c**, RHEED intensity oscillations of a SrTiO_3 (4 nm) / $\text{Sr}_3\text{Al}_2\text{O}_6$ (20 nm) / SrTiO_3 (001) heterostructure. 50 oscillations of $\text{Sr}_3\text{Al}_2\text{O}_6$ (red) and 10 oscillations of SrTiO_3 (blue) are shown. Inset: surface morphology of the heterostructure after growth. The vertical dotted lines indicate the start and end of deposition. RHEED diffraction patterns of **d**, $\text{Sr}_3\text{Al}_2\text{O}_6$ (20 nm) / SrTiO_3 (001) and **e**, SrTiO_3 (4 nm) / $\text{Sr}_3\text{Al}_2\text{O}_6$ (20 nm) / SrTiO_3 (001).

Fig. 3 Synthesis of freestanding perovskite membranes. **a**, Process schematic for heterostructure growth, oxide membrane release and transfer. **b**, Optical microscope

images of ~ 80 nm thick SrTiO_3 , $\text{La}_{0.7}\text{Sr}_{0.3}\text{MnO}_3$, and SL [20 SrTiO_3 (5 unit cell) / $\text{La}_{0.7}\text{Sr}_{0.3}\text{MnO}_3$ (5 unit cell) repeats] freestanding membranes on PDMS support. **c**, SEM image of an 80-nm-thick SrTiO_3 (left) and optical microscope image of a 2-nm-thick SrTiO_3 (right) freestanding membrane transferred onto Si wafers.

Fig. 4 Crystalline structure of epitaxial membrane films before and after release.

Reciprocal space map (RSM) of a SrTiO_3 (80 nm) film around the (103) peak before **a**, and after **b**, release from the substrate. RSM of a $\text{La}_{0.7}\text{Sr}_{0.3}\text{MnO}_3$ (80 nm) film around the (103) peak before **c**, and after **d**, release. The difference in the in-plane and out-of-plane lattice constants of $\text{Sr}_3\text{Al}_2\text{O}_6$ in **a** and **c** arises from the strain effects from the top layers. Cross-sectional HAADF-STEM images of **e**, an epitaxial and **f**, transferred $\text{La}_{0.7}\text{Sr}_{0.3}\text{MnO}_3$ / SrTiO_3 SL. Magnified images of the SL region both before and after release are also shown. The brighter layers are $\text{La}_{0.7}\text{Sr}_{0.3}\text{MnO}_3$ and the darker layers are SrTiO_3 , resulting from stronger electron scattering by the elements with higher atomic numbers ($\text{La} > \text{Sr}$). Magnified images of the SL / $\text{Sr}_3\text{Al}_2\text{O}_6$ and $\text{Sr}_3\text{Al}_2\text{O}_6$ / SrTiO_3 (001) substrate interfaces, together with schematic crystal structures, are shown in **g** and **h**, respectively, in reference to the colored boxes in **e**.

Fig. 5 Magnetic and electrical properties of $\text{La}_{0.7}\text{Sr}_{0.3}\text{MnO}_3$ single layer and SL films before and after release. **a**, Temperature dependent magnetization of a $\text{La}_{0.7}\text{Sr}_{0.3}\text{MnO}_3$ (20 nm) single layer film before (black) and after (red) release from the substrate (warming curve measured in 100 Oe in-plane field, after field cooling). **b**, Temperature dependent resistivity of the $\text{La}_{0.7}\text{Sr}_{0.3}\text{MnO}_3$ (20 nm) film before (black) and after (red) release. The temperature-dependent resistivity under perpendicular magnetic field for a SL [40 SrTiO_3 (5 unit cell) / $\text{La}_{0.7}\text{Sr}_{0.3}\text{MnO}_3$ (5 unit cell) repeats] before **c**,

and after **d**, release from the substrate. In-plane magnetization loops of the SL before **e**, and after **f**, release.

Figures

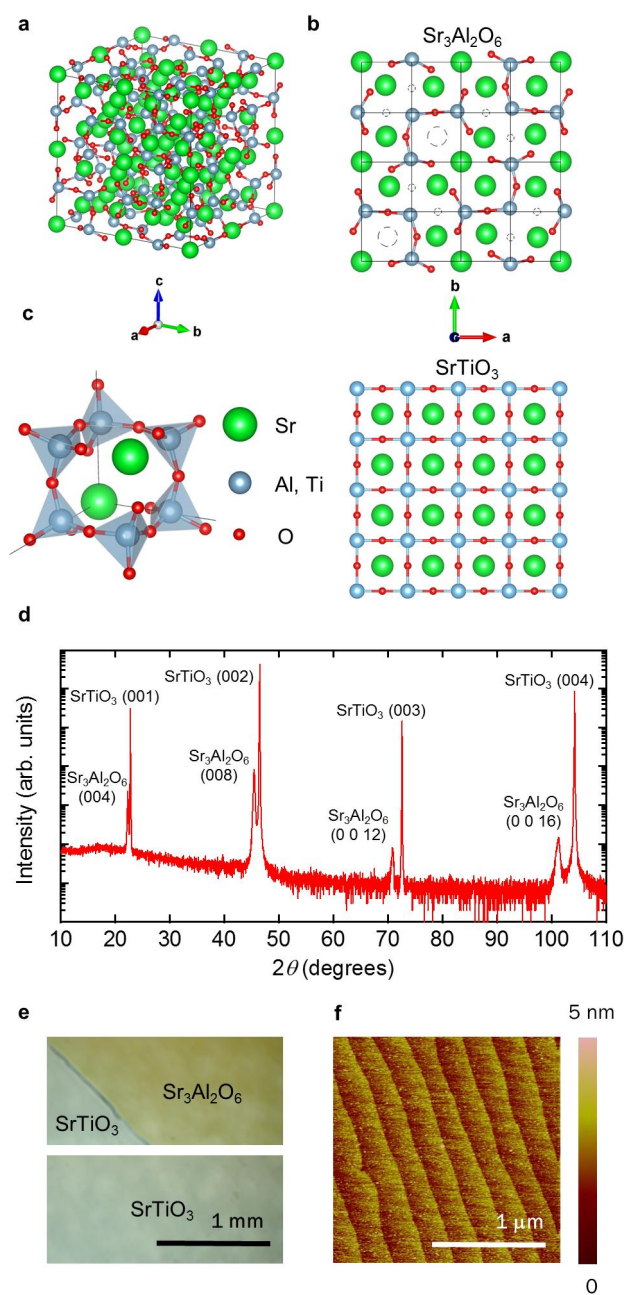


Fig. 1

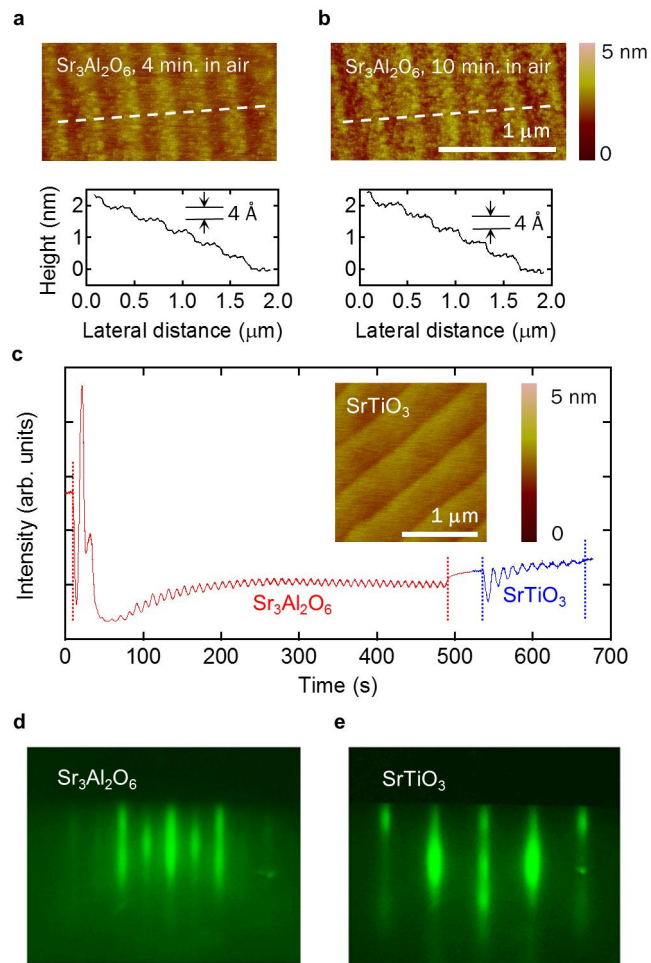


Fig. 2

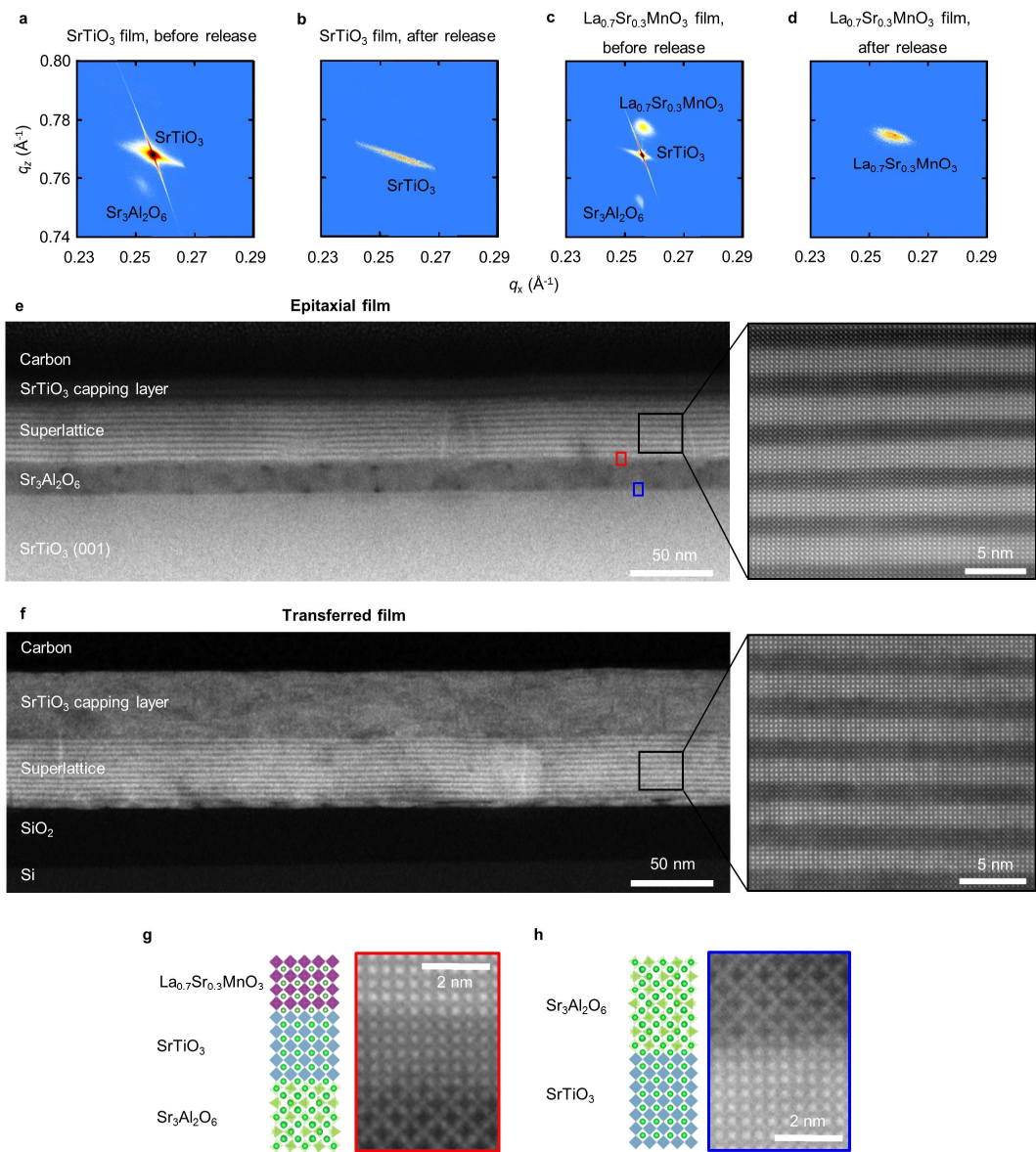


Fig. 4

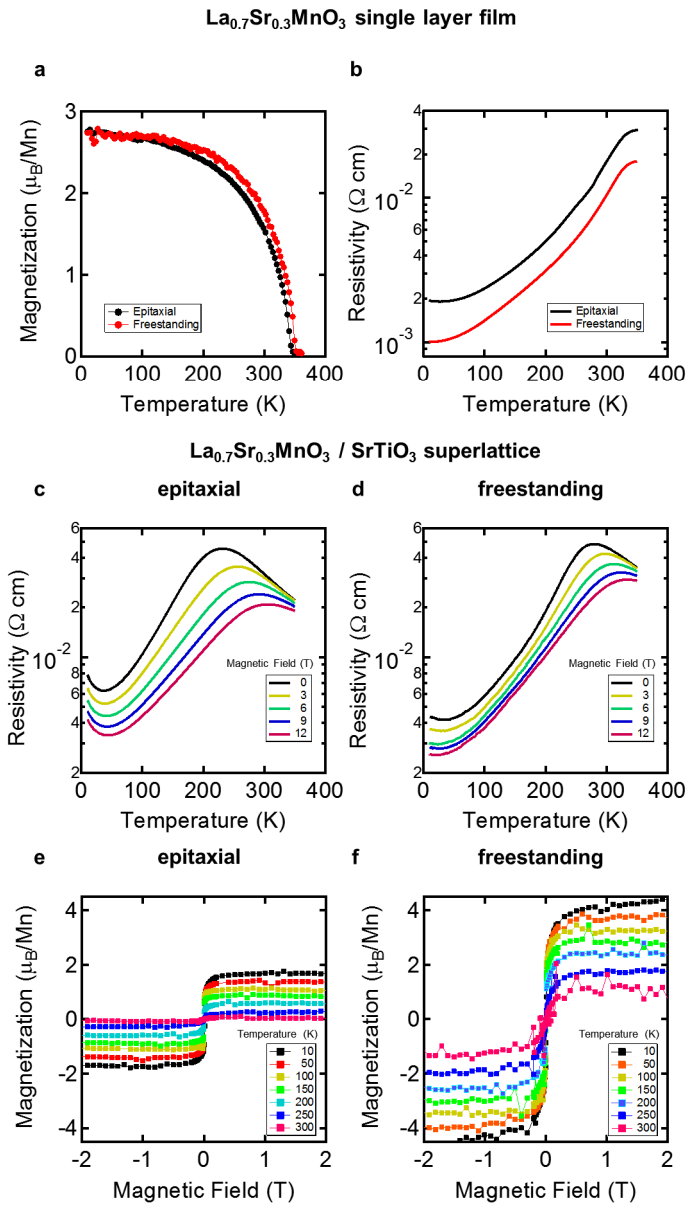


Fig. 5